Nuclear Engineering and Design 319 (2017) 163–175

Contents lists available at ScienceDirect

Nuclear Engineering and Design

journal homepage: www.elsevier.com/locate/nucengdes

Three-dimensional hydrodynamic modeling of the second shutdown system of an experimental nuclear reactor

Ludmila M. Rechiman [a,b,*], Mariano I. Cantero [a,b,c], Federico A. Caccia [a,b], Andrés Chacoma [b], Enzo A. Dari [a,b,c]

[a] Departamento de Mecánica Computacional, Centro Atómico Bariloche, Comisión Nacional de Energía Atómica, Av. E. Bustillo 9500 Centro Atómico Bariloche, S. C. de Bariloche, Río Negro, Argentina
[b] Instituto Balseiro, Universidad Nacional de Cuyo, Argentina
[c] CONICET – Consejo Nacional de Investigaciónes Científicas y Técnicas, Argentina

HIGHLIGHTS

- A CFD analysis was conducted for calculating the dynamics of the SSS of an experimental nuclear reactor.
- The numerical model solves coupled dimensionally heterogeneous systems using dynamic boundary conditions.
- The numerical model captures all the features of the physical phenomena.
- Details of 3D CFD simulation and validation procedure are outlined.
- The validated multiscale model points out that safety requirements are accomplished by the SSS of RA-10 project.

ARTICLE INFO

Article history:
Received 21 December 2016
Received in revised form 8 April 2017
Accepted 16 April 2017

2010 MSC:
00-01
99-00

Keywords:
CFD modeling
Coupling of heterogeneous systems
Free-surface numerical simulations
Validation procedure

ABSTRACT

A three-dimensional (3D) computational fluid dynamics (CFD) model is presented for the Second Shutdown System (SSS) of the experimental nuclear reactor RA-10 under design and construction by the Argentinian National Commission of Atomic Energy (CNEA). The RA-10 SSS consists on the drainage of the reflector tank surrounding the reactor core through a system of pipes in a limited amount of time solely by the action of gravity. The CFD model focuses on the 3D modeling of the reflector tank hydrodynamics and links the effects of the draining piping system through dynamics boundary conditions. The CFD model is first applied to a similar system, the RA-10 SSS Mockup, for which experimental data is available. Reasonable agreement is observed between the CFD model and the experimental observations for the RA-10 SSS Mockup. Finally, the validated CFD model is applied to the RA-10 SSS. The model results show that the performance of the RA-10 SSS meets the design requirements.

1. Introduction

The RA-10 is a new 30 MW_{th} multipurpose nuclear Research Reactor (RR) currently under design and construction by the Argentinian National Commission of Atomic Energy (CNEA) (Blaumann et al., 2013). The main objective of RA-10 will be the production of radioisotopes for medical purposes. This reactor will also provide irradiation testing facilities with neutron fluxes of the order of $10^{14}\ \frac{n}{cm^2}$ to support CNEA programs on material sciences and on nuclear fuels design. The reactor irradiation facilities are located in the heavy water reflector tank surrounding the reactor core (see Fig. 1a).

The heavy water in the reflector tank plays a central role in diminishing the neutron losses by increasing neutron re-entrance to the reactor core. The drainage of the reflector tank provides a redundant and independent safety system by allowing neutron losses from the reactor core. This is called the reactor Second Shutdown System (SSS). The reactor First Shutdown System (FSS) is based on the insertion of control rods.

Safety requirements to the RA-10 SSS demand the reflector tank to be drained to half its volume in a limited amount of time (55% of its height after 15 s) solely by the action of gravity. A three-dimensional (3D) computational fluid dynamic (CFD) model of

* Corresponding author at: Departamento de Mecánica Computacional, Centro Atómico Bariloche, Comisión Nacional de Energía Atómica, Av. E. Bustillo 9500 Centro Atómico Bariloche, S. C. de Bariloche, Río Negro, Argentina.
E-mail address: ludmila.rechiman@cab.cnea.gov.ar (L.M. Rechiman).

http://dx.doi.org/10.1016/j.nucengdes.2017.04.024
0029-5493/

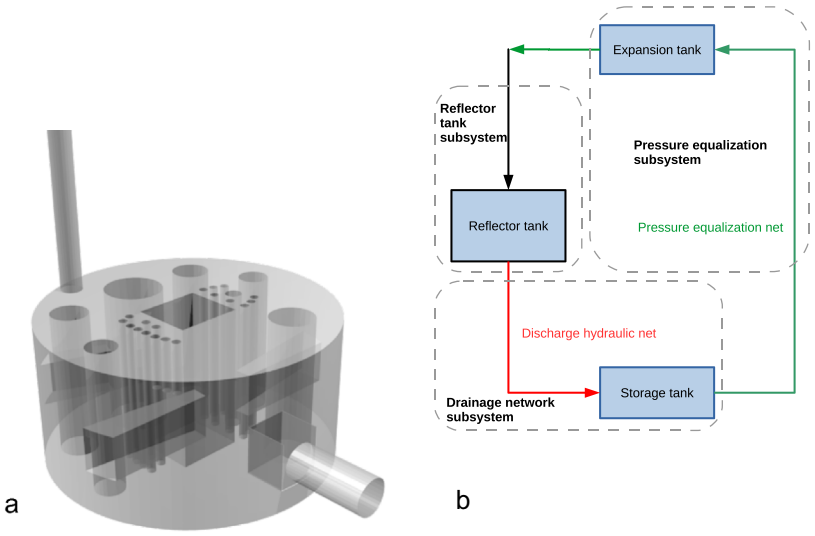

Fig. 1. (a) Reflector tank of RA-10 SSS. (b) Diagram of the RA-10 SSS decomposed into three subsystems. (Black) Reflector tank subsystem. (Red) Drainage network subsystem. (Green) Pressure equalization line subsystem. The arrows indicates the direction of the flow. (For interpretation of the references to colour in this figure legend, the reader is referred to the web version of this article.)

the RA-10 SSS has been performed in order to confirm that safety requirements are met. The RA-10 SSS is composed by three different subsystems (see Fig. 1b): the reflector tank, the drainage network subsystem and the pressure equalization subsystem.

The reflector tank drainage involves complicated 3D free surface hydrodynamics, which has to be modeled in detail. On the other hand, the flow through the drainage and pressure equalization subsystems can be simplified and described by zero-dimensional models. This decomposition and conceptualization strategy was proved to be effective in similar problems (Leiva et al., 2010; Leiva et al., 2011). The challenge in this modeling approach is to solve the coupled system (Buscaglia et al., 2005).

The hydrodynamic modeling of the RA-10 SSS implemented in this work focuses on the 3D CFD modeling of the reflector tank. The interaction between the reflector tank subsystem and the drainage and pressure equalization subsystems is made possible by implementing dynamic boundary conditions in the 3D CFD modeling using a weak-coupling technique. The 3D CFD model is first applied to the RA-10 SSS Mockup for which experimental data is available. The validated model is then employed to make predictions on the performance of the RA-10 SSS.

This work is organized as follows. Section (2) describes the main features of the RA-10 SSS. Section (3) presents the 3D CFD model of the reflector tank together with the strategy for connecting the different subsystems by dynamics boundary conditions. Section (4) presents validation results by comparing experimental observations to the 3D CFD model results of the RA-10 SSS Mockup. Section (5) presents the results of the 3D CFD model applied to the RA-10 SSS. Finally in Section (6), the conclusions are summarized.

2. General description of the RA-10 SSS.

The RA-10 SSS is mainly composed by three subsystems: the reflector tank, the discharge hydraulic net and the pressure equalization line. A simple diagram is shown in Fig. 1b. When the SSS is required to act, a manifold of six valves located in the discharge hydraulic net opens and the heavy water starts to drain solely by the action of gravity. The heavy water flows from the reflector tank through the discharge net to a storage tank located below the reactor core level. The pressure at the storage tank and over the top of the reflector tank are equalized by a pressure equalization line.

Table 1
Main characteristics of both cases: RA-10 SSS Mockup facility and RA-10 SSS.

Characteristic	Mockup	RA-10
Tank height [m]	1.215	1.000
Tank radius [m]	1.300	1.000
Diameter of upper connection [m]	0.1524	0.1524
Diameter of discharge pipe [m]	0.2540	0.2647
Net volume [m^3]	5.558	2.492
Volume of internals [m^3]	1.041	0.649
Working fluid	Light water	Heavy water
Working cover gas	Air	He
Working pressure cover gas [Pa]	92000	121300

A cover gas fills up the storage tank, the pressure equalization line and part of the expansion tank. During the performance of the SSS, the cover gas enters the reflector tank through a connection located in the upper part which is partially filled with heavy water under normal operation conditions. The system cover gas is helium.

The overall hydrodynamics of reflector tank is mainly controlled by the discharge hydraulic net and the pressure equalization line. The discharge hydraulic net imposes a pressure condition on the outflow of the reflector tank. In the same way, the equalization pressure line imposes a pressure condition on the cover gas. Incorporating the complete coupled system in the modeling for the hydrodynamics of the RA-10 SSS is mandatory.

An experimental facility has been built and operated in the past to address the hydrodynamics of a similar system to the RA-10 SSS (Villarino and Doval, 2011). In the context of the present work this facility is called RA-10 SSS Mockup. The RA-10 SSS Mockup geometry is similar but larger than the RA-10 SSS. Main features for both cases are listed in Table 1. The experimental observations of the RA-10 SSS Mockup are used to validate the 3D CFD model.

3. Three-dimensional computational fluid dynamic model for the reflector tank

The reflector tank geometry is shown in Fig. 1a. All the irradiation facilities are housed inside the reflector tank, which generate a complicated geometry of the system to model. On the other hand, as the reflector tank drains, helium fills the system generating a

free surface flow. In order to incorporate these features in the modeling process, the incompressible, isothermal, multiphase solver *interFoam* based on OpenFOAM(R) libraries Version 2.2.2 (Greenshields, 2013; Greenshields, 2013; OpenFOAM, 2016; Marquez Damián, 2013) has been selected and employed. This section describes the main features associated to the implementation of the RA-10 SSS 3D CFD model with *interFoam*.

3.1. Mathematical model

Let $t, \mathbf{U}, \alpha, \mathrm{p}, \mathbf{f}$ and $\bar{\bar{\tau}}$ be the time, the fluid velocity, the phase indicator function, the pressure, body forces and shear stress tensor respectively. The system of coupled partial differential equations that describe the free-surface flow in the reflector tank are:

$$\begin{cases} \nabla \cdot \mathbf{U} = 0 \\ \frac{\partial(\rho \mathbf{U})}{\partial t} + \nabla \cdot (\rho \mathbf{U}\mathbf{U}) = -\nabla p + \nabla \cdot \bar{\bar{\tau}} + \mathbf{f} \\ \frac{\partial \alpha}{\partial t} + \nabla \cdot (\alpha \mathbf{U}) + \nabla \cdot (\alpha(1-\alpha)(\mathbf{U}_L - \mathbf{U}_G)) = 0 \end{cases} \quad (1)$$

The interFoam solver use an Interface-Capturing Method approach based on the Volume of Fluid (VOF) technique (Hirt and Nichols, 1981). By employing this method, a single effective fluid is considered and the properties are determined by a weighing averaging with the indicator function:

$$\begin{aligned} \rho &= \alpha\rho_L + (1-\alpha)\rho_G \\ \mu &= \alpha\mu_L + (1-\alpha)\mu_G \\ \mathbf{U} &= \alpha\mathbf{U}_L + (1-\alpha)\mathbf{U}_G \end{aligned}$$

Here ρ and μ are the density and dynamic viscosity where subscript L and G denote the liquid and gas phase respectively.

3.2. Turbulent flow model

In this work two cases were considered. The first did not consider turbulence modeling, that is $\bar{\bar{\tau}}$ in Eq. (1) accounts only for viscous effects. For the second case, a two equations κ-ϵ Realizable model was used (Pope, 2000; Launder and Spalding, 1974; Shih et al., 1995) to compute $\bar{\bar{\tau}}$ in Eq. (1). The transport equations for the turbulence dissipation rate ε and the turbulent kinetic energy κ are:

$$\begin{cases} \frac{\partial \varepsilon}{\partial t} + \frac{\partial}{\partial x_j}(\mathbf{U}\varepsilon) - \frac{\partial}{\partial x_j}\left((\nu_L + \frac{\nu_T}{\sigma_\epsilon})\frac{\partial \varepsilon}{\partial x_j}\right) = C_1 S\varepsilon - \frac{C_2 \varepsilon^2}{\kappa + \sqrt{\nu\varepsilon}} \\ \frac{\partial \kappa}{\partial t} + \frac{\partial}{\partial x_j}(\mathbf{U}\kappa) - \frac{\partial}{\partial x_j}\left((\nu_L + \frac{\nu_T}{\sigma_k})\frac{\partial \kappa}{\partial x_j}\right) = \nu_T S^2 - \varepsilon \end{cases}$$

Here ν_L and ν_T are the laminar and turbulent kinematic viscosity respectively, S is the rate of strain defined as $S = \sqrt{2S_{ij}S_{ij}}$ where $S_{ij} = \frac{1}{2}\left(\frac{\partial u_i}{\partial x_j} + \frac{\partial u_j}{\partial x_i}\right)$, $C_2 = 1.9$ is a constant of the model while $C_1 = max\left\{0.43; \frac{\eta}{5+\eta}\right\}$ where $\eta = \frac{S\kappa}{\varepsilon}$. The remaining constants are $\sigma_\kappa = 1.0$ and $\sigma_\varepsilon = 1.2$.

3.3. Spatial discretisation of the problem

The simulation domain for the 3D subsystem can be seen in Fig. 2. The spatial discretisation of the problem has been done using a non-structured mesh of tetrahedrons.

The surface and volumetric meshes have been generated by NETGEN under Salome Version 7.2.0 (S. OPEN CASCADE, 2013). Salome has been selected based on the fact that it handles efficiently the Boolean operations between bodies needed to produce the intrincated geometry seen in Fig. 2.

The NETGEN mesh generator allows to obtain a suitable mesh without slivers, which are badly distorted elements which render the mesh unsuitable for calculations (Dari and Buscaglia, 1994; Rechiman et al., 2014).

A reference mesh was used for the calculations in both cases, RA-10 SSS Mockup case and RA-10 SSS case. Main features of meshes are listed in Table 2. Moreover, computations on a refined mesh were also carried out in order to evaluate the grid convergence of solution.

3.4. Discretisation schemes of operators

The temporal term of the Eq. (1) was solved by an implicit and 2nd order accurate method, backward differencing scheme.

An *adaptive time step control* was employed. Along calculations, the time step is chosen so it does not exceed the local Courant threshold defined by the user.

The maximum Courant number was bounded in a value $Co^{max} = 0.95$ in all calculations. This value was set in order to ensure stability while keeping an affordable time for simulations.

Regarding how differential operators are solved, the integration and interpolation methods were specified. For the gradient terms *Gauss linear*, while for laplacian terms *Gauss linear corrected*. For the convective term of the momentum equation, a *Gauss linearUpwindV* scheme was used, while for the convective term involved in the transport equation of the indicator function a *Gauss vanLeer* scheme was employed.

3.5. Boundary conditions for the 3D model of the reflector tank

The boundary conditions (BC) applied on each *physical surface* are sum up in Table 3. Slip BC has been applied on the walls due to the thickness of boundary layers are much smaller than the typical dimensions of the tank. The system of Eq. (1) is rewritten in terms of a field defined by $p_{rgh} = p - \rho\vec{g}\cdot\vec{x}$, where p is the pressure, $\vec{g}$ is acceleration of gravity and $\vec{x}$ denotes the coordinates of the point of interest. The last is done in order to avoid the dependence with depth. By using the p_{rgh} field, the formulation of the BC is simplified.

The *totalPressure* BC was used to set the boundary values in the Gas Connection patch. The reference pressure involved in this BC has been set to the working pressure, $p_{rgh} = 92,000 - \rho\vec{g}\cdot\vec{x}$ Pa in the RA-10 SSS Mockup case and $p_{rgh} = 121300 - \rho\vec{g}\cdot\vec{x}$ Pa in the RA-10 SSS case.

On the other hand, the *groovyTotalPressure* BC has been employed to set the values in the discharge patch. This BC is part of a set of libraries developed by Gschaider (2013). The implementation of this dynamic BC allows to program an expression for the reference pressure p_0. The pressure p_0 is determined by the coupling with the hydraulic discharge net and then will be equal to $p_0(t) = p_{coupling}(t) - \rho\vec{g}\cdot\vec{x}$. This dynamic BC allows to refresh the value of the boundary in every time step according to the zero-dimensional model of the piping subsystem calculated with information of the previous time-step. This is called a weak-coupling approach. This BC holds until the average of the indicator function at discharge patch is $<\alpha>= 0.5$. When gas enters to discharge duct and is below $<\alpha>= 0.5$, the hydraulic net decouples from the model and the working pressure of the gas will be acting on the discharge patch.

3.5.1. Model for draining subsystem

A discharge hydraulic net conducts the reflector liquid to a storage tank. This drainage network subsystem imposes a pressure condition given by $p_{coupling}(t)$ over the outflow of the subsystem of the reflector tank. The piping subsystem is composed by a main duct (MD) with an internal diameter D_{MD}, several concentrated pressure losses represented by $\sum K_i^{MD}$, a manifold of six branches $\sum K_i^V$ each of one has a length L_V which contain a spherical valve

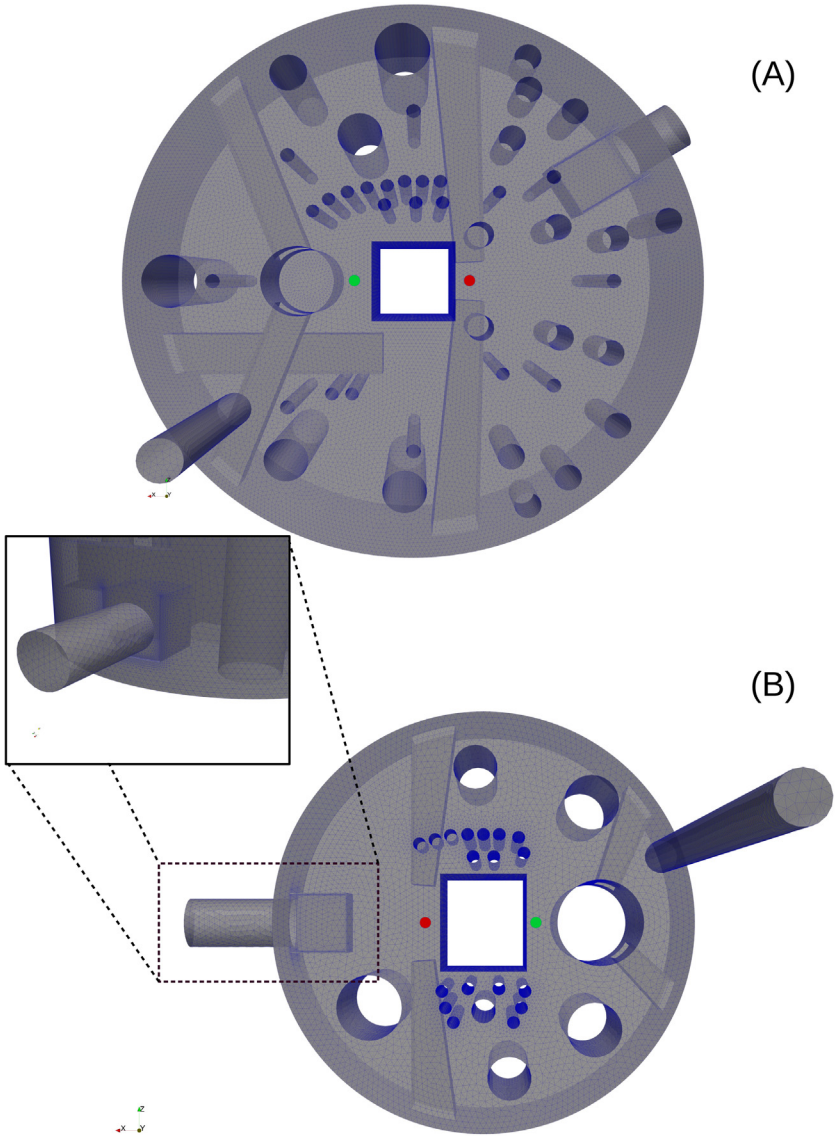

Fig. 2. (A) Unstructured mesh of tetrahedrons of the RA-10 SSS Mockup tank. Surface mesh is displayed. (B) Unstructured mesh of tetrahedrons for the geometrical configuration of interest of RA-10 SSS. Surface mesh is displayed. (Inset) Detail of the outlet connected to the hydraulic net. (Green dots) Location of the virtual ruler (I). (Red dots) Location of the virtual ruler (II). (For interpretation of the references to colour in this figure legend, the reader is referred to the web version of this article.)

Table 2
Main properties of meshes.

Mesh characteristic	Reference mesh Mockup	Fine mesh Mockup	Mesh RA-10	Fine mesh RA-10
N tetrahedrons	1447277	3931189	1092550	2307495
Faces	3025881	7993705	2252932	4715007
Internal Faces	2763227	7731051	2117268	4514973
Volume [m^3]	5.558	5.558	2.492	2.492
Max. Aspect ratio	7.95	6.68	6.67	6.55
Min. Vol. [m^3]	6.09×10^{-9}	6.12×10^{-9}	1.61×10^{-9}	5.09×10^{-9}
Max. Vol. [m^3]	3.48×10^{-5}	1.12×10^{-5}	2.19×10^{-5}	6.64×10^{-6}
Non-orth Max. angle [°]	67.87	67.79	60.37	61.48
Max. Skewness	0.81	0.77	0.68	0.76

with an associated pipe of diameter D_V, and finally a sudden expansion to the storage tank. The hydraulic net has an effective height given by the difference in the locations of the inlet and the outflow of the net $z_{net} = (z_{\text{outlet}} - z_{\text{inlet}})$. A zero-dimensional analysis of the hydraulic net allows to estimate the pressure at discharge patch ($p_{coupling}(t)$) given by Eq. (2).

$$\begin{aligned} p_{coupling}(t) = p_{out} + (z_{\text{outlet}} - z_{\text{inlet}})\rho_l g + \ldots \\ \ldots + \rho_l \frac{V_{\text{MD}}^2(t)}{2}\left[f_{MD}\frac{\sum(L_i^{MD})}{D_{\text{MD}}} + \sum K_i^{MD} - 1\right] + \ldots \\ \ldots + \rho_l \frac{V_V^2(t)}{2}\left[f_V \frac{L_V}{D_V} + \sum K_i^V + 1\right] \end{aligned} \quad (2)$$

Table 3
Boundary condition applied on each *physical surface*.

Physical surface	BC **U**	BC p_{rgh}	BC α
Discharge patch	$\frac{\partial \mathbf{U}}{\partial n} = 0$	$p_0(t) - \frac{1}{2}\lvert\mathbf{U}^2\rvert$	$\frac{\partial \alpha}{\partial n} = 0$
Gas Connection patch	$\frac{\partial \mathbf{U}}{\partial n} = 0$	$p_0 - \frac{1}{2}\lvert\mathbf{U}^2\rvert$	$A\frac{\partial \alpha}{\partial n} + B\alpha = C$
Walls	$\hat{t}\cdot(\bar{\bar{\tau}}\cdot\hat{n}) = 0$	$\frac{\partial p_{rgh}}{\partial n} = 0$	$\frac{\partial \alpha}{\partial n} = 0$

Here $p_{coupling}(t)$ is the pressure at the outlet of the tank, p_{out} is the pressure at the discharge of the net, which is coincident with the working gas pressure, z_{outlet} is the height of the outlet of the net, z_{inlet} is the height of the inlet of the net, $\sum K_i^{MD}$ and $\sum K_i^{V}$ are the effective local hydraulic resistances along the main duct and at each valve's branch, f_{MD} and f_V are the Darcy friction factors at the main duct and at each branch of the valve's manifold respectively, D_{MD} and D_V are the diameters of the pipes of the main duct and at the branch, $\sum L_i^{MD}$ and L_V are the corresponding lengths of the pipes to calculate the distributed friction factors and $V_{\text{MD}}(t)$ and $V_{\text{V}}(t)$ are the average velocities of the flow at main duct and at valve's branch. The values for the reference net used along all the computations presented in this work are listed in Table 4.

In the present model, it is considered the possibility that one valve could fail to open when the action of the SSS is required, then five effective parallel paths for fluid flow of the manifold are taken into account. It is also considered that the valves present no hydraulic resistance when they are fully open. It should be remarked that it is assumed that the net full of liquid starts the evolution with a null mass flow and instantly reaches the stationary regime.

3.5.2. Model for pressure equalization subsystem

The upper part of the reflector tank is connected to the pressure equalization subsystem (Fig. 1).

The pressure difference between the beginning of the equalization line located in the storage tank (Point A) and the end of it located in the upper part of the reflector tank (Point C) is given by Eq. (3).

$$\frac{p_A - p_C}{\rho_G g} = (z_C - z_A) + \frac{V_{AB}^2}{2g}\left[\frac{f_{AB}L_{AB}}{D_{AB}^{He}} + \sum_i K_{AB}^i\right] + \ldots$$
$$\ldots + \frac{V_{BC1}^2}{2g}\left[\frac{f_{BC1}L_{BC1}}{D_{BC1}^{He}} + \sum_i K_{BC1}^i\right] + \frac{V_{BC2}^2}{2g}\left[\frac{f_{BC2}L_{BC2}}{D_{BC2}^{He}} + \sum_i K_{BC2}^i\right] \quad (3)$$

In Eq. (3) the point B is located in the expansion tank, while points $C1$ and $C2$ refer to the same duct that changes the radial dimension along its path. In the RA-10 SSS Mockup case the pressure equalization subsystem does not exists and the ambient pressure acts on top of the tank. In the RA-10 SSS case, the parameters for the equalization pressure subsystem are displayed in Table 5.

A post-facto analysis of this subsystem points out that the pressure drop along this line is negligible. Then, the working gas pressure acting on top of the tank as a BC for the 3D CFD model is a good approximation.

Table 4
Main geometrical characteristics of the discharge hydraulic piping system.

Characteristic	Mockup	RA-10
p_{out} [Pa]	92000	121300
$\sum K_i^{MD}$ [l]	4.6	2.8
$\sum K_i^{V}$ [l]	0.7	0.7
$\sum L_i^{MD}$ [m]	8.5	14.5
L_V[m]	1.0	0.9
$(z_{\text{outlet}} - z_{\text{inlet}})$ [m]	−6.3	−7.7
D_{MD} [m]	0.254	0.265
D_V [m]	0.102	0.067

Table 5
Parameters for the pressure equalization subsystem.

Characteristic	RA-10
p_{out} [Pa]	121300
$\sum_i K_{AB}^i$ [l]	4.3
$\sum_i K_{BC1}^i$ [l]	1.9
$\sum_i K_{BC2}^i$ [l]	1.0
L_{AB} [m]	15.7
L_{BC1} [m]	15.3
L_{BC2} [m]	3.5
$(z_s - z_e)$ [m]	8.4
D_{AB}^{He} [m]	0.080
D_{BC1}^{He} [m]	0.108
D_{BC2}^{He} [m]	0.168

3.6. Parallel calculations

The computations were carried out in a cluster of workstations connected by a Gigabit Ethernet network. Each node is an Intel(R) Core(TM) i7-3820 CPU 3.60 GHz. To make the domain decomposition (DD), the graph partitioning method based on the Scotch algorithm was used (Pellegrini, 2009). A performance analysis has been carried out. This analysis indicates that using 28 processors on 7 nodes and applying the Scotch method to carry out the DD, is the optimum option for the problem at hand (Rechiman et al., 2014).

4. 3D CFD model validation

4.1. RA-10 SSS Mockup experimental data

The position of the free-surface has been measured in a local manner in the RA-10 SSS Mockup facility (Garnero, 2014; Rechiman et al., 2015). This information was used in the validation procedure of the 3D CFD model. The position of the interface was track on a vertical ruler along the depth of the RA10-SSS Mockup tank by using a video camera. It is important to point out that the time evolution of the system starts ($t = 0$) when the free-surface cross the junction between the upper part of the reflector tank with the pressure equalization line.

4.2. Cases of study for validation procedure

Numerical simulations were carried out for two cases of study in order to get a model which enables to capture all the physics features with accuracy without requiring an excessive computing time. The following cases have been computed:

1. Case I: System of Eq. (1) using the two equation model $\kappa - \varepsilon$ Realizable to compute $\bar{\bar{\tau}}$.
2. Case II: System of Eq. (1) computing $\bar{\bar{\tau}}$ accounting only for viscous effects.

These two numerical experiments allow to quantify the unevenness in the solution between a complex model (Case I) and a self-effacing model (Case II).

4.3. Description of events in the RA-10 SSS Mockup case

The initial state of the system is shown in Fig. 3. It can be seen that the reflector tank is full of liquid as well as part of the pressure equalization line. The height of this line is 1.5 m.

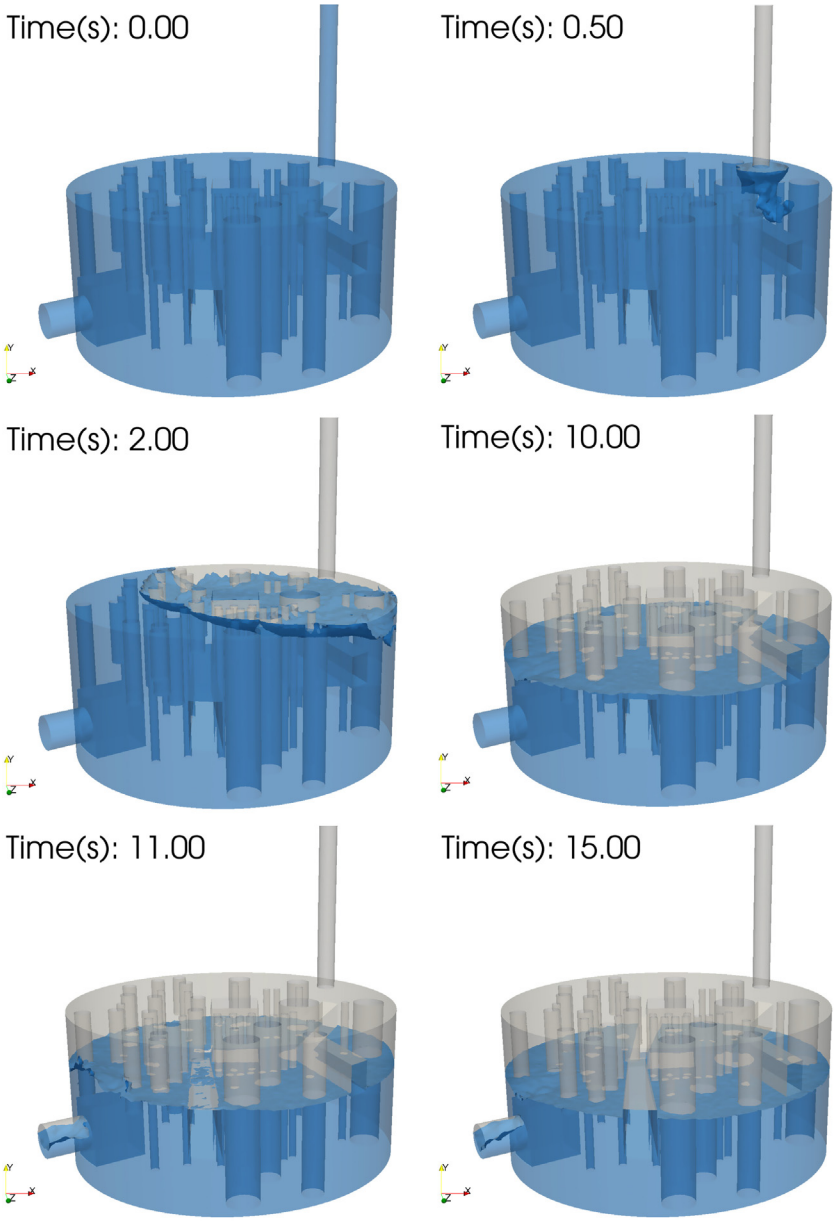

Fig. 3. Time evolution sequence of the free-surface inside the tank predicted by the coupled model applied to the RA-10 SSS Mockup geometry.

When the valves in the discharge hydraulic net are open, the liquid contained in the pressure equalization line fully drains in approximately ~ 0.35 s. After the plug fall down, a violent liquid jet with a mean velocity of 7.3 $\frac{m}{s}$ and a maximum velocity of 11 $\frac{m}{s}$, impacts over one of the cold neutron beams and a bowl-shaped depression is created. The depression depth is nearly 0.45 m at time 0.50 s.

A wide wave starts to travel towards the direction where is located the discharge pipe. Diffraction and reflection patterns are generated while the wave interact with the tank internals. The subsequent waves can reach 23 cm of amplitude. The first wave reaches the opposite side at 3 s of time evolution and reflects. After this time the waves start to diminish their amplitude until the free-surface of the liquid is nearly smooth with minor distortions.

Ten seconds after the system starts to evolve, the coupled 3D CFD model predicts the establishment of a gas pocket at discharge duct. When this happens, the working gas pressure will be acting on discharge duct. Moreover, the hydraulic net will no longer influence the discharge of the tank. Due to the change in the output pressure, the mass flow drops and the hydraulic net discharges in a two-phase regime. When the gas pocket is formed, the effective liquid cross section diminishes down to 35% and is located as a horizontal half moon on the bottom of the pipe. Moreover, from now on the discharge dynamic get slower, and a change in the slope of the draining curve is observed.

4.4. Mass flow, free-surface and velocity results of RA-10 SSS Mockup case

Fig. 4 shows the computed mass flow curves for the two cases of study in the RA-10 SSS Mockup. Both cases are in perfect accord during the acceleration part (first 0.5 s), when the plug flows from top into the reflector tank. Moreover, they describe in a similar manner the global behavior of the discharge process, although the inclusion of the turbulent effect produce a smoother evolution than the case without it. This may be caused by the fact that the

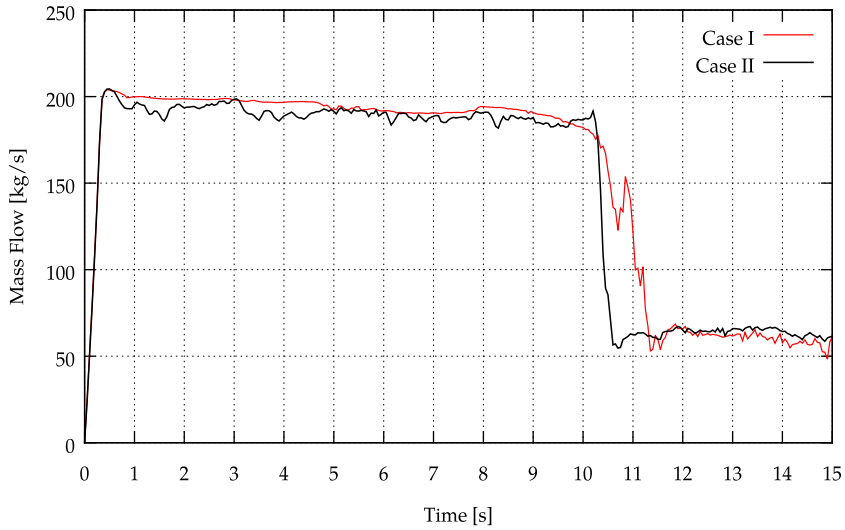

Fig. 4. Mass flow of liquid phase at discharge patch for Cases (I) and (II) for the coupled model applied to the RA-10 SSS Mockup geometry. The sudden drop in the mass flow at $t \sim 10$ s is caused by the entrance of gas to the discharge duct. When the average of the indicator function at discharge patch is below $< \alpha >= 0.5$ the discharge hydraulic net is decoupled from the model.

turbulent kinematic viscosity could be up to $\nu_T = 0.025\ \frac{m^2}{s}$, which is four order of magnitude larger than the fluid kinematic viscosity. Then, the larger kinematic viscosity may attenuate flow fluctuations in the region where the mass flow is computed.

At time $t \sim 10$ s the entrance of air is produced on discharge duct. This fact breaks the depression condition imposed by the hydraulic net over the tank. Then, the hydraulic net is decoupled from the model. Due to the sudden change of the indicator function in the cross section of the duct, the middle point of the transition was chosen as a criterion for decoupling the hydraulic net.

The solution of the spatial distribution of the free-surface has been compared for the two cases. In particular, Fig. 5 displays contours for a fixed value $\alpha = 0.5$. Reasonable agreement can be seen for the two cases except when the gas pocket is established at discharge pipe.

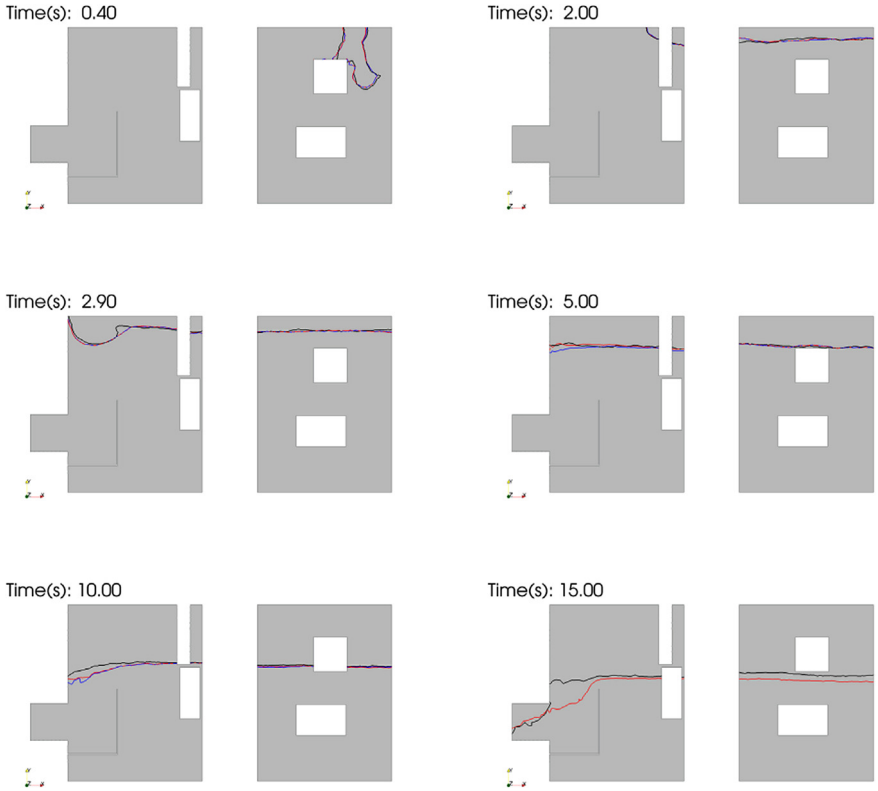

Fig. 5. Time evolution sequence of the free-surface predicted by the coupled model applied to the RA-10 SSS Mockup geometry. The results are shown in a cut along the diameter of the tank. (Red) Case I. (Black) Case II. (Blue) Additional simulation taking into account the surface tension effect. (For interpretation of the references to colour in this figure legend, the reader is referred to the web version of this article.)

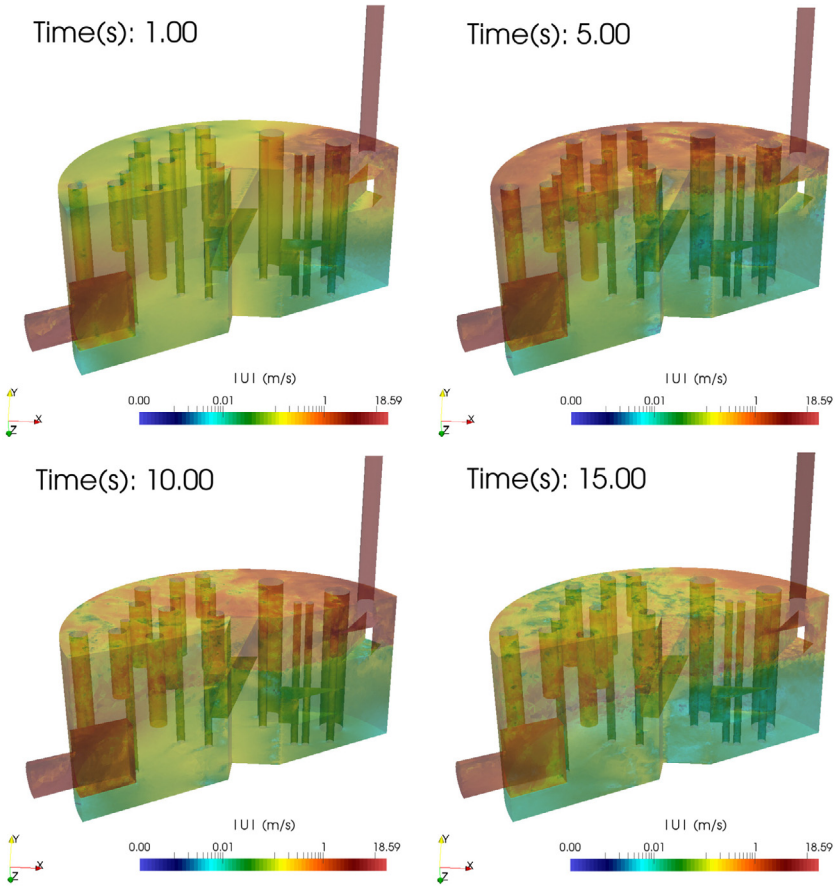

Fig. 6. Modulus of velocity field developed in the RA-10 SSS Mockup geometry.

Fig. 6 shows a time sequence of the modulus of the velocity field for the effective fluid within the RA-10 SSS Mockup tank. Despite the large dimensions of the tank, no dead water regions exist within it. Then, possible reductions of the calculation domain are not allowed. On the other hand, the average velocity at discharge patch is $\sim 4.5\ \frac{m}{s}$, while the mean velocity of gas in

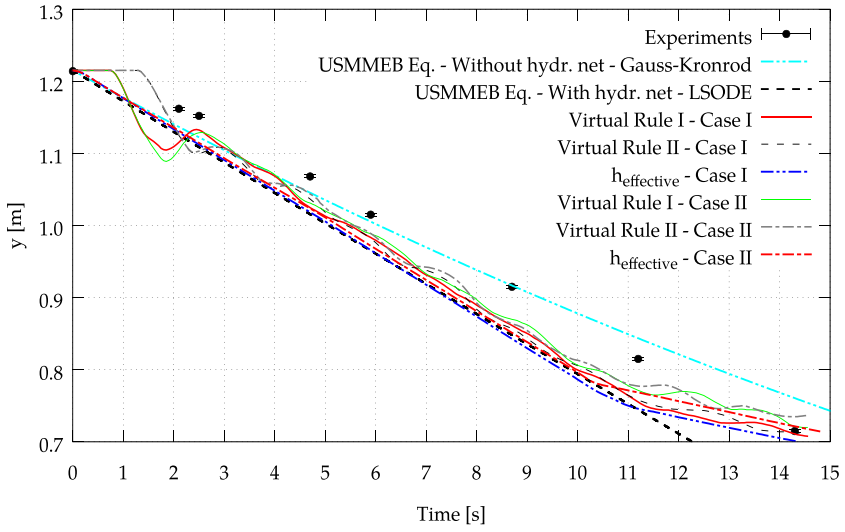

Fig. 7. Draining curves of the RA-10 SSS Mockup facility. The position of the free-surface was computed for the first 15 s of time evolution. The time $t = 0$ s corresponds to the moment when the free-surface cross the connection with the pressure equalization line. (Black) Experimental measurements. (Cyan dotted line) Unsteady-state macroscopic mechanical energy balance (USMMEB) for a kindred model of the problem. Solution for Eq. (4) without the coupling with the hydraulic discharge net solved by a Gauss–Kronrod quadrature integrator. (Thick black dotted line) USMMEB given by Eq. (5) including the coupling with the hydraulic discharge net solved by an Octave Livermore ordinary differential equation LSODE integrator. (Solid red line) Local measurement of free-surface position on a virtual ruler located at position I for the Case I. (Thin dotted black line) Local measurement of free-surface position on a virtual ruler located at position II for the Case I. (Dotted blue line) Global estimation of free-surface position for Case I. (Solid green line) Local measurement of free-surface position on a virtual ruler located at position I for the Case II. (Dotted gray line) Local measurement of free-surface position on a virtual ruler located at position II for the Case II. (Dotted red line) Global estimation of free-surface position for Case II. (For interpretation of the references to colour in this figure legend, the reader is referred to the web version of this article.)

the gas connection line is $\sim 17\ \frac{m}{s}$ with an associated Mach number of $Ma = 0.05$. The last is consistent with the incompressibility assumption.

4.5. Validation and verification of the coupled 3D-0D CFD model in the RA-10 SSS Mockup case

In order to evaluate the neutronic impact on the negative reactivity insertion caused by the removal of the reflector, the time evolution of the position of the free-surface is determined.

Fig. 7 displays the time evolution of the free-surface. The position of the free-surface has been determined in a *local manner* calculating the interface position on virtual rulers located near the reactor core (see Fig. 2) for the numerical experiments associated with Case (I) and Case (II).

The local estimators present a delay of 1 s for virtual rulers located at position (I), while for virtual rulers located at position (II) the delay is equal to 1.8 s. The delay is attributed to the time the wave takes to reach these positions. Afterwards, the local estimators oscillate because of the wave motion.

Alternatively, the location of free-surface has been determined in a *global manner* calculating in an indirect way a mean effective position $h_{effective}$ of the free-surface by using the mass conservation law between the cross-section of the tank and the discharge duct.

The global estimator for the liquid height remaining inside the tank is a decreasing linear monotonic function up to 10 s. At that time, a slope change occurs due to the fact that the lighter fluid starts to enter through the discharge pipe and then the hydraulic net is decoupled.

For both cases, the local and global estimation for the location of the free-surface are alike.

We also compare the numerical results with previous experimental data of RA-10 SSS Mockup reported in Garnero (2014) and Rechiman et al. (2015). The curves obtained with the present coupled 3D-0D CFD model behave in a similar manner to the experimental one specially at $t > 10$ s. During the initial evolution,

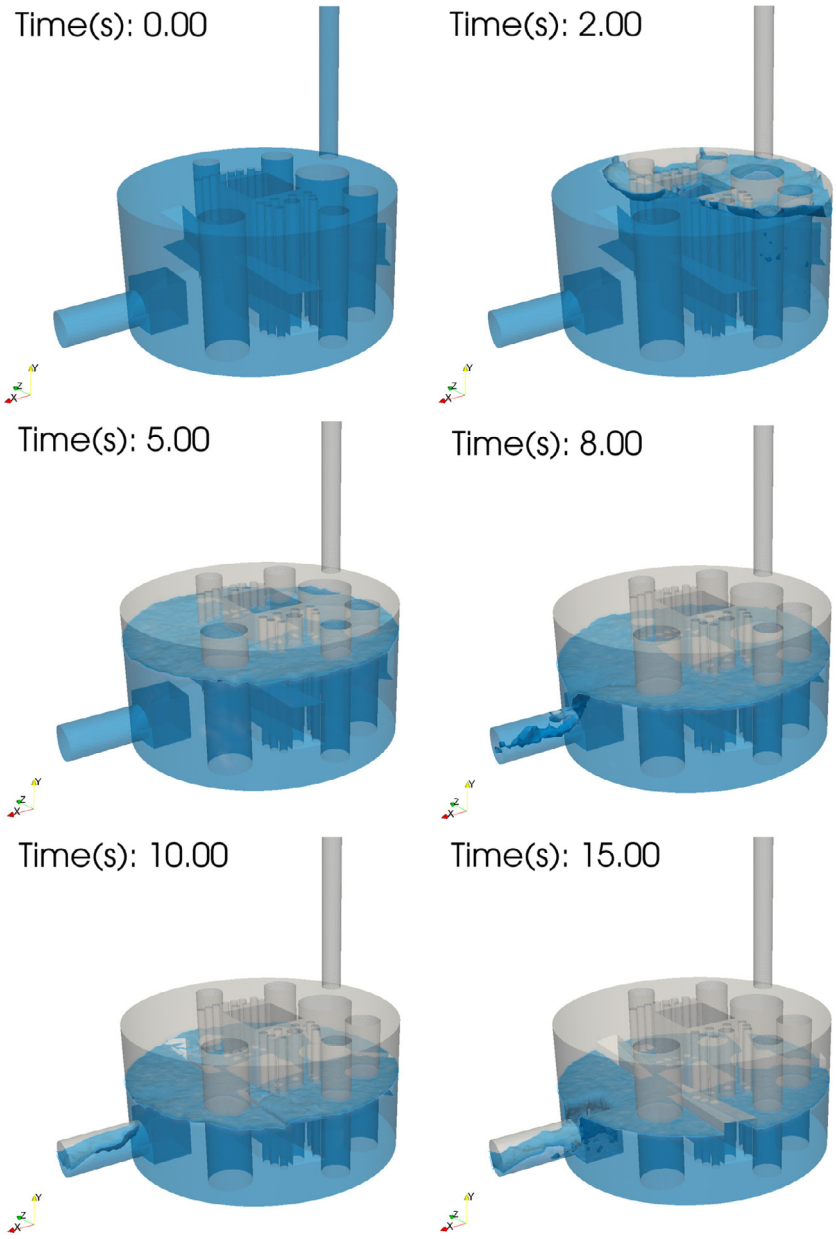

Fig. 8. Time evolution sequence of the free-surface inside the tank predicted by the coupled model applied to the RA-10 SSS geometry.

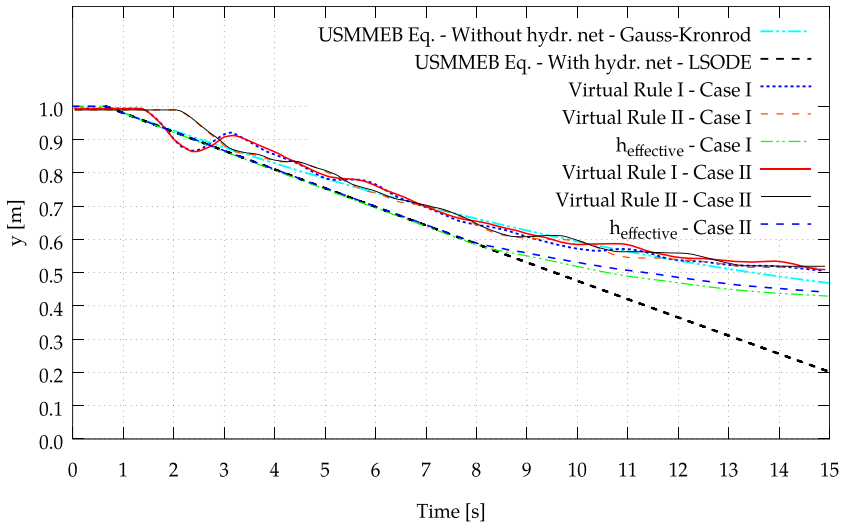

Fig. 9. Draining curves for the RA-10 SSS case. The position of the free-surface was computed for the first 15 s of time evolution. The time $t = 0$ s corresponds to the moment when the valves are open. (Cyan dotted line) Unsteady-state macroscopic mechanical energy balance (USMMEB) for a kindred model of the problem. Solution for Eq. (4) without the coupling with the hydraulic discharge net solved by a Gauss–Kronrod quadrature integrator. (Thick black dotted line) USSMEB given by Eq. (5) including the coupling with the hydraulic discharge net solved by an Octave Livermore solver for ordinary differential equations LSODE integrator. (Solid red line) Local measurement of free-surface position on a virtual ruler located at position I for the Case I. (Thin black line) Local measurement of free-surface position on a virtual ruler located at position II for the Case I. (Dash blue line) Global estimation of free-surface position for Case I. (Dotted blue line) Local measurement of free-surface position on a virtual ruler located at position I for the Case II. (Dash red line) Local measurement of free-surface position on a virtual ruler located at position II for the Case II. (Dash dot green line) Global estimation of free-surface position for Case II. (For interpretation of the references to colour in this figure legend, the reader is referred to the web version of this article.)

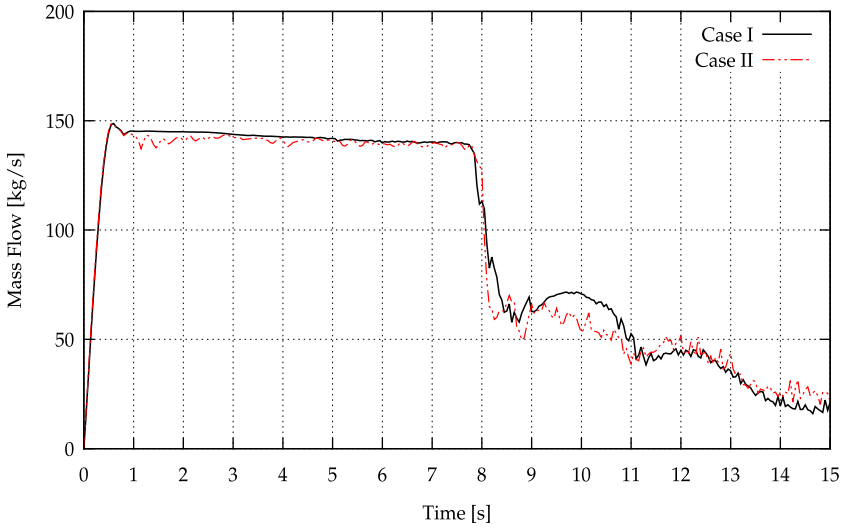

Fig. 10. Mass flow of liquid phase at discharge patch for the RA-10 SSS case. (Black) Case I. (Red) Case II. At $t \sim 8$ s the hydraulic net is decoupled from the model when the average of the indicator function at discharge patch is below $< \alpha >= 0.5$.

a mismatch is evident. The main reason of the discrepancy between the model and the measured height of water is due to the time it takes the initial emptying wave to reach the measuring location in the experiments.

The different approaches to estimate the location of the free-surface were compared with a simple model based on the unsteady-state macroscopic mechanical energy balance (USMMEB) (Bird et al., 2002; Rechiman et al., 2014; Rechiman et al., 2016). Two extreme cases have been considered: A) The simple model without the hydraulic net attached to the tank. B) The simple model coupled in a dynamic manner with the hydraulic discharge net subsystem.

For case A, let $t_{draining}$ be the time to drain an initial liquid height h_0 contained in a cylindrical tank of radius R_{tank} with a circular orifice of radius $R_{discharge}$ located at a height $y_{discharge}$. Following Bird et al. (2002), the draining time for the tank without the hydraulic net attached to it is given by Eq. (4).

$$t_{draining} = -\sqrt{\frac{(N-2)h_0}{2g}} \int_0^1 \frac{d\eta}{\sqrt{\eta - \frac{2\eta^{(N-1)}}{N}}} \tag{4}$$

In Eq. (4) g is the gravity acceleration, $N = \frac{R_{tank}^4}{R_{discharge}^4}$ and $\eta = \frac{h}{h_0}$.

For case B, the previous model was modified by assuming that a pressure p_{top} is acting on top of the tank, and that a pressure imposed by a hydraulic net is acting on the discharge orifice represented by $p_{coupling}(t)$. The latter case is expressed by Eq. (5).

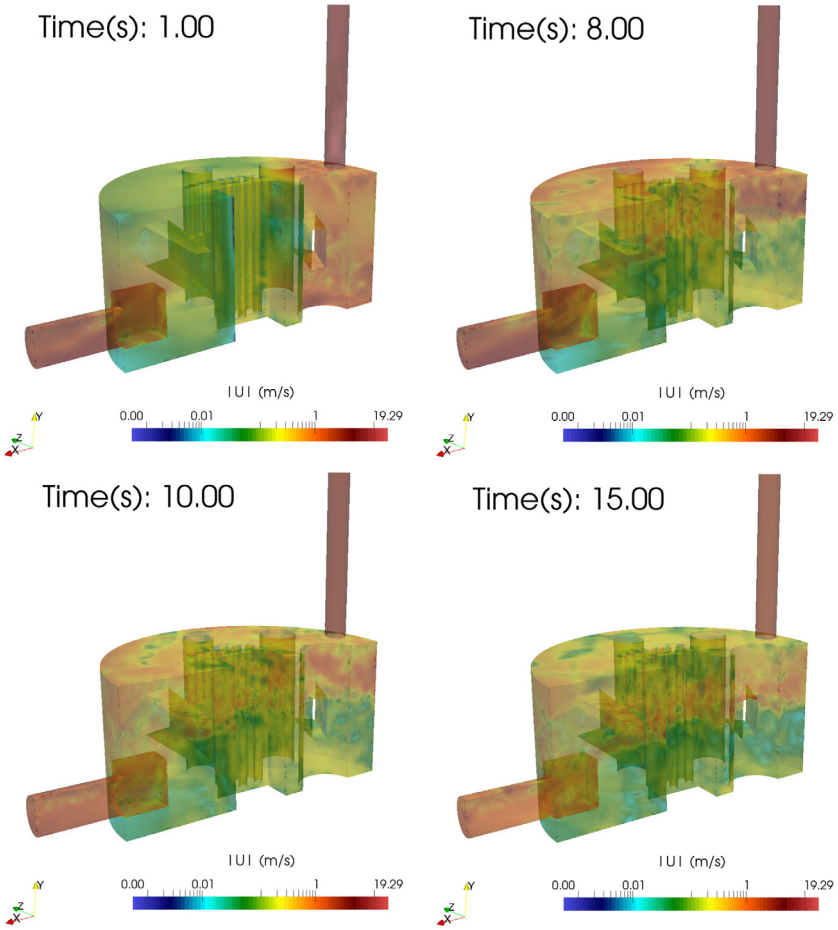

Fig. 11. Modulus of velocity field developed in the RA-10 SSS geometry.

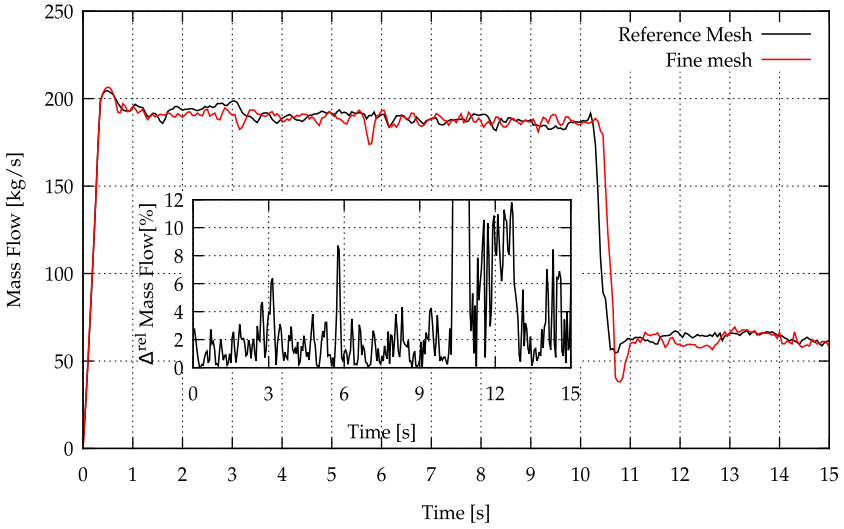

Fig. 12. Mass flow of liquid phase at discharge patch with the configuration of Case II. (Black) Reference mesh. (Red) Fine Mesh. (Inset) Relative difference between the solutions. (For interpretation of the references to colour in this figure legend, the reader is referred to the web version of this article.)

$$h(t)\frac{d^2h}{dt^2}+\frac{1}{2}\left[1-\left(\frac{R_{tank}}{R_{discharge}}\right)^4\right]\left(\frac{dh(t)}{dt}\right)^2+g(y_{discharge}+h(t))=\frac{(p_{coupling}(t)-p_{top})}{\rho_l} \quad (5)$$

In Eq. (5) the $p_{coupling}(t)$ is given by Eq. (2).

Fig. 7 shows that curves represented by Eqs. (4) and (5) enclose the former results of the 3D-0D CFD model. It can be clearly seen that the net acts like a pump which accelerates the draining flow. In consequence, the time required to emptying the same amount of

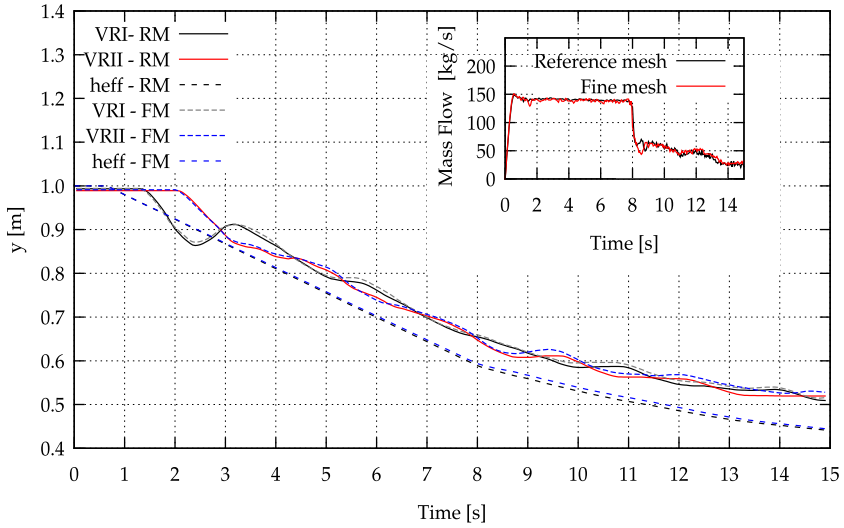

Fig. 13. Draining curves for the RA-10 SSS case in the reference mesh and in a fine mesh. The position of the free-surface was computed for the first 15 s of time evolution. (Solid black line) Local measurement of free-surface position on a virtual ruler (VR) located at position I for the Case I in the reference mesh (RM). (Solid red line) Local measurement of free-surface position on a VR located at position II for the Case I in the RM. (Dash black line) Global estimation of free-surface position for Case I in the RM. (Dotted gray line) Local measurement of free-surface position on a VR located at position I for Case I in the fine mesh (FM). (Dotted blue line) Local measurement of free-surface position on a VR located at position II for the Case I in the FM. (Dash blue line) Global estimation of free-surface position for Case I in the FM. (For interpretation of the references to colour in this figure legend, the reader is referred to the web version of this article.)

liquid is faster than if the net would not been there for these set of parameters. It is important to remark that when the air entrainment at discharge pipe occurs, the USMMEB solution is no longer valid.

A key issue not addressed at the moment is the effect of the spatial discretization on the solution. A detailed mesh convergence analysis is shown in Appendix A.

5. Results in the geometry of interest of RA-10 SSS

The validated 3D-0D CFD model was applied to the geometry of interest of RA-10 SSS. Two cases have been studied, the same two cases than for RA-10 SSS Mockup.

Fig. 8 shows the 3D time evolution of the free-surface. After the plug fall into the tank the wave motion vanish and the free-surface is nearly plannar. The draining with a nearly plannar surface continue until the gas first enter to discharge patch at $t \sim 7.8$ s. A distortion of free-surface in the surrounding of discharge box occurs. Finally at time $t = 15$ s, the free-surface is slightly above the upper edge of discharge box at $y \sim 0.53$ m . The complete process can be visualized in the Supplemental material (Rechiman, 2017). These set of simulations show that the overall motion of flow within the tank is similar to the RA-10 SSS Mockup case.

Fig. 9 shows the discharge curves for the RA-10 SSS geometry. The time $t = 0$ s indicates the moment when the valves are open. The pressure equalization line connection is fully drained during the first $t \sim 0.65$ s. The local estimators show an oscillating behavior due to wave motion generated by the falling plug of liquid from the pressure equalization line. The evolution of the local estimators is retarded due to the time that takes the wave to reach each virtual ruler.

On the other hand, the global estimators are coincident with the simple model with hydraulic net up to a time of 8 s. These predictions are no longer valid for times beyond $t > 7$ s. This is due to the fact that a systematic depression is formed in the surrounding of the discharge box. Then, the solution of mass flow is affected by a diminishing of cross-section area involved in global calculation which was considered coincident with the cross-section of the tank.

At time $t \sim 7.8$ s the gaseous phase starts to enter to the discharge pipe while the surface is slightly perturbed by the wave motion. Furthermore, the evolution of different estimators and the solution of the simple model without the discharge net have the same trend for $t > 8$ s.

Fig. 9 also shows that the position of the interface after 15 s of evolution is in the middle of the tank height $y \sim 0.53$ m, slightly above the upper edge of discharge box. These results answer the main query about the studied configuration.

Fig. 10 shows the mass flow for the two computed cases. It can be seen that the mass flow reaches a plateau in a value of $\dot{m} = 144 \frac{kg}{s}$. At $t \sim 7.8$ s a gas pocket is formed in the discharge duct.

The modulus of velocity field is displayed in Fig. 11. The region of liquid flow with highest velocity is in the surrounding of the discharge box where the mean velocity of the flow at discharge pipe is $V_{discharge} = 4 \frac{m}{s}$ similar to RA-10 SSS Mockup.

The mesh convergence analysis of the computational model is developed in Appendix A.

6. Conclusions

In the present work we have presented and discussed the results of a free-surface 3D CFD model applied to two geometrical configurations, the RA-10 SSS Mockup geometry and the RA-10 SSS geometry.

There were two main objectives in this paper. The first one was to validate the 3D-0D coupled methodology by comparing our results with theoretical and experimental data available for the RA-10 SSS Mockup configuration. The second one was to present a detailed analysis of the SSS performance for the RA-10 case.

We have implemented a robust model using OpenFOAM(R) suite which allows to make massive three-dimensional simulations with the current available facilities in order to contribute to a design stage of the SSS.

We used this tool to show an assessment of the dynamical behavior in the RA-10 SSS Mockup. It was proved that the coupling strategy applied to the complete system can reproduce the overall behavior regarding the draining dynamics of the reflector tank for

the 15 s of time evolution. The simulations produced a complex free-surface behavior in two moments: after the falling plug and when air entrainment is produced on discharge duct.

We have determined the free-surface location by using local and global estimators. Both approaches indicate similar results and reasonable agreement exists with experimental data measured in a local manner. The results also show that the gas pocket creation as well as the decoupling moment of the hydraulic net can not be predicted by any simple model and a full coupled three-dimensional model is necessary.

We have applied the same framework developed for the RA-10 SSS Mockup model to the geometry of interest of RA-10 SSS case. Calculations show that after 15 s of time evolution the liquid level remaining inside the tank is slightly above the upper edge of discharge box $y \sim 0.53$ m. This result suggest that the safety requirements are accomplished by the analyzed SSS.

Acknowledgments

The authors acknowledge support from RA-10 project and Comisión Nacional de Energía Atómica (CNEA). We thanks to CIMEC from Universidad Nacional del Litoral for their support when endeavoring the first steps with OpenFOAM. We would also like to thank all the contributors in CFD online and OpenFOAM community.

Appendix A. Mesh convergence analysis

RA-10 SSS Mockup case

In order to evaluate if the mesh resolution used for the calculations is good enough, the same problem similar than Case (II) was computed but with a refined mesh. The refined mesh is composed by 728283 points and 3931189 tetrahedrons. The general characteristics of this mesh are listed in Table 2.

Fig. 12, shows the drained mass flow calculated with the reference mesh and with the refined mesh. A good agreement exists between them. Moreover the integral of the mass flow along the 15 s of time evolution was calculated for both cases. The discharged mass of liquid computed with the reference mesh is $m = 2234.41$ kg while for the case computed with the refined mesh is 2234.72 kg. Then the discrepancy in the solution of the mass leaving the tank is 0.02%. These results suggest that the solution is converged for the reference mesh used along the present work.

RA-10 SSS case

The Case (I) was computed but using a refined mesh which characteristics are displayed in Table 2. Fig. 13 shows in a comparative manner the calculations with the reference mesh and with the refined mesh. Regarding the position of the interface as well as the mass flow computed, it can be seen that results of both cases are alike. The integral in time of the mass flux was also calculated. Using the reference mesh the result is $m^{RM}_{drained} = 1418\ kg$, while for the refined mesh is $m^{FM}_{drained} = 1413\ kg$. These results suggest that the solutions calculated with the reference mesh are converged.

Appendix B. Supplementary data

Supplementary data associated with this article can be found, in the online version, at http://dx.doi.org/10.1016/j.nucengdes.2017.04.024.

References

Bird, R., Stewart, W., Lightfoot, E., 2002. Transport Phenomena,. John Wiley & Sons.
Blaumann, H., Vertullo, A., Sánchez, F., Brollo, F., Longhino, J., 2013. RA-10: A New Argentinian Multipurpose Research Reactor. International Atomic Energy Agency.
Buscaglia, G.C., Dari, E.A., Arnica, D.L., Larreteguy, A.E., Mazufri, C., 2005. Computational fluid dynamics throughout the design process in nuclear applications. In: Applications of Computational Mechanics in Structures and Fluids. CIMNE, A Serie of Handbooks on Theory and Engineering Applications of Computational Methods.
Dari, E., Buscaglia, G., 1994. Mesh optimization: how to obtain good unstructured 3D finite element meshes with not-so-good mesh generators. Struct. Optimiz. 8, 181–188.
Garnero, I., 2014. Segundo sistema de parada Validación del CFD para el drenaje del tanque reflector. Technical report RA-10 project, INVAP, CL-INV-RA-10-0300-2-004. <http://www.invap.com.ar>.
Greenshields, C.J., 2013. User Guide, Vol. Version 2.2.2, CFD Direct Ltd.
Greenshields, C.J., 2013. Programmers Guide, Vol. Version 2.2.2, CFD Direct Ltd.
Gschaider, B.F., 2013. Swak4Foam reference, Manual.
Hirt, C., Nichols, B., 1981. Volume of Fluid (VOF) method for the dynamics of free boundaries. J. Comp. Phys. 39, 201–225.
Launder, B., Spalding, D., 1974. The numerical computation of turbulent flows. Comput. Methods Appl. Mech. Eng. 3 (2), 269–289.
Leiva, J., Blanco, P.J., Buscaglia, G.C., 2010. Iterative strong coupling of dimensionally heterogeneous models. Int. J. Numer. Methods Eng. 81, 1558–1580.
Leiva, J., Blanco, P.J., Buscaglia, G.C., 2011. Partitioned analysis for dimensionally-heterogeneous hydraulic networks. Multiscale Model Simul. 9 (2), 872–903.
Marquez Damián, S., 2013. An Extended Mixture Model for the Simultaneous Treatment of Short and Long Scale Interfaces (Ph.D. thesis). Universidad Nacional del Litoral.
OpenFOAM, 2016. <http://www.openfoam.org/>.
Pellegrini, F., 2009. Contributions au partitionnement de graphes paralléle multi-niveaux Ph.D. thesis. Université de Bordeaux I.
Pope, S., 2000. Turbulent Flows. Cambridge University Press.
Rechiman, L.M., 2017. Supplemental material, discharge dynamics of second shutdown system of RA-10 reactor.
Rechiman, L.M., Cantero, M.I., Dari, E.A., 2014. Contributions of CFD to the Analysis of the Second Shutdown System of the RA-10 Research Reactor. International Group On Research Reactors IGORR Conference.
Rechiman, L.M., Cantero, M.I., Dari, E.A., 2014. Hydrodynamic transient assessment of a draining tank. Mecánica Computacional Vol XXXIII.
Rechiman, L., Cantero, M., Dari, E.A., 2015. Multiscale model of the Mockup of second shutdown system of RA-10 reactor. Technical report RA-10 project, IN-ATN40MC-02/2015.
Rechiman, L., Cantero, M., Caccia, F., Dari, E.A., 2016. Validation of multiscale model of the second shutdown system of an experimental nuclear reactor. Mecánica Computacional. Asociación Argentina de Mecánica Computacional XXXIV 2199–2215.
Shih, T., Liou, W., Shabbir, A., Yang, Z., Zhu, J., 1995. A new $\kappa - \epsilon$ eddy viscosity model for high Reynolds number turbulent flows. Comput. Fluids 3, 227–238.
S. OPEN CASCADE, 2013. The Open Source Integration Platform for Numerical Simulation. Salome tutorial. User's guide, SALOME.
Villarino, E., Doval, A., 2011. INVAP's Research Reactor Designs. Science and Technology of Nuclear Installations, 490391.